ACS APPLIED MATERIALS & INTERFACES

Article

Core-Levels, Band Alignments, and Valence Band States in CuSbS for Solar Cell Applications

Thomas J. Whittles, Tim D. Veal, Christopher N. Savory, Adam W. Welch, Francisco Willian de Souza Lucas, James T. Gibbon, Max Birkett, Richard J. Potter, David O. Scanlon, Andriy Zakutayev, and Vinod R Dhanak

Just Accepted

ACS Publications

Core-Levels, Band Alignments, and Valence Band States in CuSbS$_2$ for Solar Cell Applications

Thomas J. Whittles[†], Tim D. Veal[†], Christopher N. Savory[‡,§], Adam W. Welch[‖], Francisco Willian de Souza Lucas[‖], James T. Gibbon[†], Max Birkett[†], Richard J. Potter[⊥], David O. Scanlon[‡,§,#], Andriy Zakutayev[‖], and Vinod R. Dhanak[,†]*

[†]Stephenson Institute for Renewable Energy and Department of Physics, University of Liverpool, Liverpool L69 7ZF, United Kingdom

[‡]Department of Chemistry, University College London, Christopher Ingold Building, London WC1H 0AJ, United Kingdom

[§]Thomas Young Centre, University College London, Gower Street, London WC1E 6BT, United Kingdom

[‖]National Renewable Energy Laboratory, Material Science Center, 15013 Denver W Parkway, Golden, CO 80401, USA

[⊥]Department of Mechanical, Materials and Aerospace Engineering, School of Engineering, University of Liverpool, Liverpool L69 3GH, United Kingdom

[#]Diamond Light Source Ltd., Diamond House, Harwell Science and Innovation Campus, Didcot, Oxfordshire, OX11 0DE, United Kingdom

KEYWORDS

$CuSbS_2$, copper antimony sulfide, XPS, DFT, thin film solar cells, band alignments, density of states

ABSTRACT

The earth-abundant material $CuSbS_2$ (CAS) has shown good optical properties as a photovoltaic solar absorber material, but has seen relatively poor solar cell performance. To investigate the reason for this anomaly, the core-levels of the constituent elements, surface contaminants, ionization potential, and valence band spectra are studied by x-ray photoemission spectroscopy (XPS). The ionization potential and electron affinity for this material (4.98 eV and 3.43 eV) are lower than for other common absorbers, including $CuIn_xGa_{(1-x)}Se_2$ (CIGS). Experimentally corroborated density functional theory (DFT) calculations show that the VBM is raised by the lone pair electrons from the antimony cations contributing additional states when compared with indium or gallium cations in CIGS. The resulting conduction band misalignment with CdS is a reason for the poor performance of cells incorporating a CAS/CdS heterojunction, supporting the idea that using a cell design analogous to CIGS is unhelpful. These findings underline the critical importance of considering the electronic structure when selecting cell architectures that optimize open-circuit voltages and cell efficiencies.

INTRODUCTION

The drive to discover and develop materials for use in terawatt-scale thin film photovoltaics (PV) has grown somewhat in recent years, due to the necessity of eliminating environmentally harmful or economically unfeasible elemental components from their production, as is the case with the current market leaders, cadmium telluride (CdTe) or copper indium gallium diselenide (CIGS)[1–4]. One attractive family of materials for this purpose is the ternary copper chalcogenides, taking the general form $Cu_mM_nCh_x$ (M = Sb, Bi; Ch = S, Se), developed as analogues to CIGS, replacing trivalent In and Ga with Sb or Bi[1,5,6].

Here, the compound $CuSbS_2$ (CAS) is of interest, which has previously demonstrated appealing photovoltaic properties[7]. With scarcity and world demand for antimony being significantly lower than for indium[6], as well as having almost equivalent ionic radii[8], this metal could prove a good substitute, both economically and in terms of PV properties. Long known as the naturally occurring mineral chalcostibite, its potential as a solar absorber was only realized in 2001[5], with the first cell being constructed in 2005[9]. Since then, it has demonstrated a solar-matched band gap of ~1.5 eV[5,10,11], inherent p-type conductivity due to the dominant copper vacancy[5,12,13], and absorption stronger than both CIGS and copper zinc tin sulfide (CZTS)[7], which is another popular earth-abundant absorber. CAS has a relatively low melting point of ~540°C[2,13], and so is amenable to crystallization at lower temperatures. CAS has thus far been successfully grown in thin film and nanoscale form by many and varied deposition methods, both physical (thermal evaporation[2,14,15] and sputtering[3,4,16]) and chemical (spray pyrolysis[12,17], chemical bath[5,9,10,18], spin coating[13], electrodeposition[11,14], solution processing[19] and solvo-/hydro-thermal[20–22]), leading to continued interest in the material. Beyond its use as a solar absorber, interest is also maintained in CAS because of its potential use in other areas of

semiconductor applications, such as supercapacitors[23], dye-sensitized solar cells[24], or electrodes in batteries[25].

Despite this, solar cell performance thus far has been severely limited and the shortcomings of the literature reports on device properties have been previously ackowledged[3]. There have been very few reports of fully built PV devices and those that do exist commonly report no[8,9,18], or very low (<2%)[2,4,13,15] efficiencies. The efficiency record currently stands at only 3.22%[26], with another study reporting a near-record efficiency of 3.13%[11]. Despite over a decade of research, recent reports still acknowledge that further investigation into device fabrication and characterization is required[7,15]. This is especially the case, given that these record efficiency devices utilize similar architectures, which all involve the use of problematic CdS.

Although antimony takes the trivalent oxidation state in CAS, like Ga/In does in CIGS, CAS does not form in the tetrahedral chalcopyrite crystal structure like CIGS[27]. Instead, CAS forms in a structure (shown in Figure 1 and generated from x-ray diffraction data[28]) that is somewhat distorted by the stereochemically active antimony lone pair electrons, which do not take part in bonding[29]. The copper atoms are 4-fold coordinated to sulfur in almost regular tetrahedra, whereas the antimony atoms are 5-fold coordinated to sulfur in a distorted square-based pyramid arrangement. The lone pair electron density is then directed into the void between the SbS_5 pyramid units[30]. With two Sb-S bonds being much longer than the other three[28] (shown as grey in Figure 1), the crystal structure is said to be layered through the plane intersecting these bonds[4]. Consequently, there are two inequivalent sulfur sites, one which is coordinated to two Cu and three Sb atoms, and the other which is coordinated to two Cu and two Sb atoms[1] (labelled S1 and S2 in Figure 1, respectively). This crystallography, which is very dissimilar from that of CIGS or

CZTS[3], leads to differences in the characteristic properties and electronic structures, which are thought to be the cause of the poor device performances.
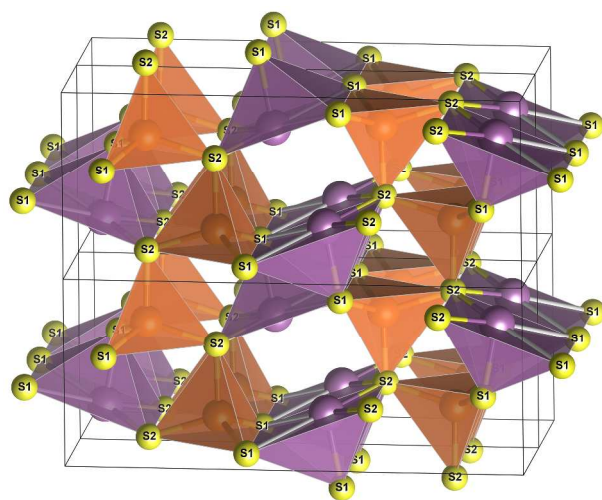
Figure 1. Crystal structure of chalcostibite $CuSbS_2$, showing the individual atoms of Cu (orange), Sb (purple) and S (yellow). The inequivalent sulfur coordination sites are marked.

This article presents a full x-ray photoemission spectroscopy (XPS) analysis of $CuSbS_2$, including core-levels, valence band spectra, band edge positions, and the effects of surface cleaning and contamination. Complexities in the spectra can mask the surface contamination, the effects of which are important to recognize because they can impact the electronic properties. The valence band findings are corroborated with theoretical density of states calculations to explain how the bonding nature of the material affects the position of the VBM. This gives rise to a low ionization potential, which is partly responsible for the poor efficiencies seen in $CuSbS_2$ solar cells, due to poor conduction band alignment with the commonly used window layer, CdS.

METHODS

Experimental Section. Films of phase-pure polycrystalline $CuSbS_2$ (~1.5 μm thickness) were synthesized by co-sputtering from Sb_2S_3 and Cu_2S targets on bare and Mo-coated soda lime glass

substrates heated to $350^{\circ}C$[16]. To improve the quality of the $CuSbS_2$ material, some of the resulting thin films were annealed at 455°C for 11 hours in a tube furnace under flow of N_2 in the presence of sacrificial Sb_2S_3 powder[3]. The annealing was preceded by a 100°C water vapor removal step for 30 minutes and a 60 minute heating step; it was followed by a 5 hour cooling step down to room temperature. The results for the annealed $CuSbS_2$ thin films are presented below, whereas the results for the as-deposited films are provided in the Supporting Information. More details about the synthesis[16] and annealing[3] of the same $CuSbS_2$ thin films have been previously reported.

Raman spectra were acquired using a Horiba Scientific Jobin-Yvon LabRam HR confocal Raman microscope. This consisted of a confocal microscope coupled to a single grating spectrometer, equipped with a longpass filter and a CCD detector. Spectra were measured using an incident wavelength of 514.5 nm from an argon ion laser with a CCD exposure time of 30 s and 5 acquisitions. Before measurements, the spectrometer was calibrated to the zero order and the 520 cm^{-1} Raman line of silicon.

Optical transmission and specular reflection spectra were recorded at 4 and 300 K and for photon energies of 0.3 to 2.4 eV at an angle of incidence of 11° to the surface normal using a combined reflection-transmission accessory in a Bruker Vertex 70v Fourier-transform infrared (FTIR) spectrometer. The low temperature was obtained using an Oxford Instruments CFV2 continuous-flow helium cryostat. The vacuum pressures were 2 mbar for the optical path in the spectrometer and 1×10^{-6} mbar in the sample environment of the cryostat. The procedure for reduction of the transmission and reflection spectra to obtain absorption spectra is described elsewhere[31].

XPS measurements were performed in a standard ultrahigh vacuum (UHV) chamber operating at a base pressure of less than 2×10^{-10} mbar with hydrogen as the main residual gas. Samples were attached to the sample plates by spot welding tantalum straps across the sample edges. This also provided an electrical connection between the CAS films and the spectrometer. In vacuo sample cleaning was performed by means of Ar^+ ion sputtering and a radiative heating stage. The core-level electronic structure, valence band density of states and secondary electron cutoff (SEC) were measured using monochromated Al Kα x-ray radiation, operating nominally at 250 W, details of which, including the calibration of the spectrometer, are described elsewhere[32].

Samples were sputtered and annealed in order to remove surface contaminants including oxides and hydrocarbons which inevitably form due to handling in ambient atmosphere. During cleaning, the samples were monitored by XPS and were considered to be clean when the C 1s peak and peaks due to antimony oxide were no longer visible on the survey spectra. Such cleanliness was achieved by grazing angle (20°) sputtering with 500 eV Ar^+ in 5 minute steps (30 minutes total) followed by annealing at 200°C for 60 minutes. Relatively low energy and a grazing angle of incidence were used in order to minimize damage. This cleaning facilitated the measurement of a more representative surface of $CuSbS_2$ and hence, prevented the valence band (VB) spectra being overwhelmed by signal from the contamination. It is noted however, that a full set of XPS spectra was taken prior to surface cleaning to demonstrate the changes taking place and also the tendency of oxide formation at the surface of this material.

Prior to cleaning, the main C 1s signal, due to contaminant carbon, was found to have a binding energy (BE) of 284.7 eV and was deemed to have either experienced no, or very minimal charging due to this binding energy being observed for contaminant carbon on this material previously.[2,8,18,33] However, after subjecting the sample to surface cleaning, the very

poor signal to noise ratio for the C 1s peaks meant that this peak could no longer be used for charge correction. Instead, it is believed the copper in CAS should be affected least by cleaning, and as such, the copper $2p_{3/2}$ peak should demonstrate the same BE throughout. Therefore, the spectra were calibrated using the Cu $2p_{3/2}$ BE of CAS prior to cleaning, which was measured to be 932.0 eV.

Computational Modeling. All periodic Density Functional Theory (DFT) calculations in this article were performed through the Vienna Ab Initio Simulation Package (VASP). The screened hybrid functional HSE06 was used for geometry optimization and the density of states calculations. HSE06 includes 25% Hartree-Fock exchange, which is screened with a parameter of w = 0.11 bohr^{-1}, with 75% exchange and full correlation from the Generalized Gradient Approximation (GGA) functional PBE. This method has been used successfully in previous reports on $CuSbS_2$ and is described more fully there[1,7]. The projector-augmented wave method was used to describe the interaction between valence and core electrons, and scalar-relativistic pseudopotentials were used. A cut-off energy of 375 eV and a Γ-centered k-point mesh of $4 \times 7 \times 2$ were used in all calculations, determined to be sufficient to converge the total energy to within 1 meV/atom. A convergence criterion of 0.01 eV Å^{-1} on the forces per atom was used for the geometry optimization, and the cut-off energy was increased to prevent errors arising from Pulay stress.

RESULTS AND DISCUSSION

The Raman spectrum for $CuSbS_2$ is shown in Figure 2 and reveals a single intense peak at 335 cm^{-1}, which is characteristic of the chalcostibite phase[34]. Also observed are weaker Raman modes at 101, 140 and 164 cm^{-1}, along with two weak features around 220 and 260 cm^{-1}, all of which have been reported or observed previously[2]. The Raman modes corresponding to Sb_2S_3[35],

CuS[36] and the other stoichiometries of copper antimony sulfide, Cu_3SbS_3[37], Cu_3SbS_4[38] and $Cu_{12}Sb_4S_{13}$[34], are not present in the spectrum. This supports previous x-ray diffraction (XRD) measurements of $CuSbS_2$ prepared using an identical method[3], in finding that the $CuSbS_2$ is phase-pure.
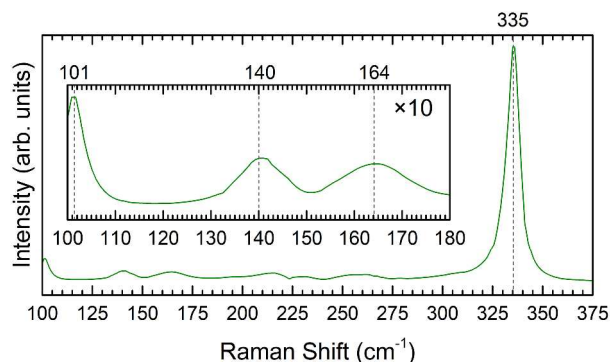
Figure 2. Raman spectrum for the CAS sample.

Core-Level XPS. XPS can be used as a powerful tool for determining oxidation states in materials. In addition, it can also identify and determine the effects of surface contamination, which can be detrimental to device performance. Unfortunately, complexities in the spectra can lead to misinterpretations, which led to the adoption of the fitting procedure applied below. Further discussion of these complexities with regards to CAS is given in the Supporting Information.

The pre- and post-cleaning survey spectra are shown in Figure 3. Peaks for the expected elements of copper, antimony and sulfur from the material are visible, along with peaks from carbon and oxygen; not unexpected because of hydrocarbon contamination from exposure to atmosphere, which then subsequently reduced after cleaning. Sodium peaks were also found, but did not decrease on cleaning, suggesting that the sodium has diffused through from the glass, as has been seen in similar materials. Further discussion of the nature and effects of sodium with the corresponding spectra can be found in the Supporting Information.
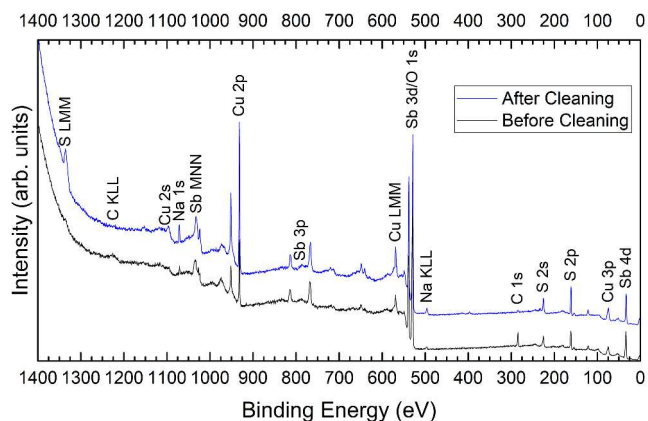
Figure 3. XPS survey spectra for the CAS sample before and after surface cleaning.

The following is an analysis of the high resolution spectra for the regions of interest in this material. The fitted binding energies and FWHM of the core-levels are summarized in Table 1. All spectra were fitted using Voigt functions after Shirley background subtraction. Further details of the analysis, with the associated spectra, and values for surface stoichiometry can be found in the Supporting Information.

The Cu 2p spectra were fitted with one doublet separated by 19.8 eV[39] and with an area ratio of 1:2, attributed to Cu^+ in $CuSbS_2$. The FWHM of the Cu $2p_{1/2}$ peak is somewhat broader than that of the Cu $2p_{3/2}$ peak due to Coster-Kronig effects[40]. Because charge correction was achieved using the Cu $2p_{3/2}$ peak, all spectra are nominally similar, and a comparison before and after cleaning is shown in Figure 4. It can be seen that no discernible change occurred during the cleaning process, showing no oxidation of the copper in the material after growth and demonstrating the quality of the material, as copper oxidation has been noted previously[21].
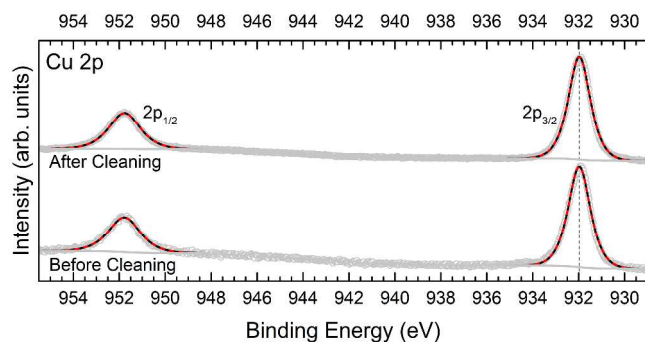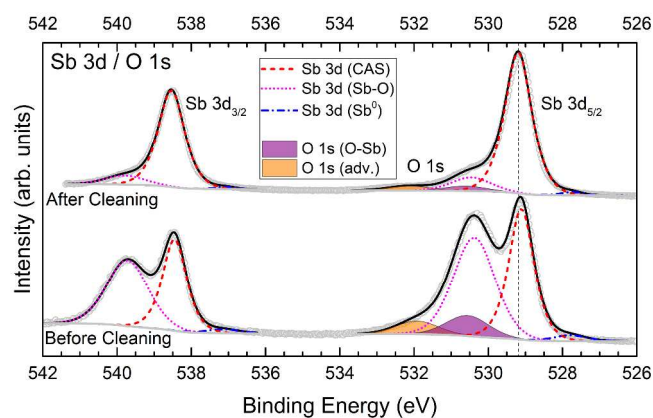
Figure 4. XPS spectra for the Cu 2p region of the CAS sample before and after surface cleaning. Fitted peaks shown in red and peak envelope shown in black.

The overlapping regions of Sb 3d and O 1s were fitted according to the procedure detailed in the Supporting Information, and the spectra before and after cleaning are shown in Figure 5. It can be seen that prior to cleaning, two distinct peaks are visible in the Sb $3d_{3/2}$ region, with a shoulder to the lower binding energy side of the lower peak (~537 eV). These features were fitted with three Sb 3d doublets, and the remaining intensity in the Sb $3d_{5/2}$ region, relating to O 1s emission, was fitted with two peaks. The strongest, sharpest antimony doublet (red dash) was attributed to Sb^{3+} in $CuSbS_2$, sharpest because of the high crystallinity of the intentionally grown material. The doublet at highest binding energy (pink dot) was attributed to antimony in a Sb-O environment. It is thought that this oxide consists predominantly of Sb_2O_3, as the trivalency of antimony is maintained and the binding energy is in agreement with literature values[41]; however, it is possible that the oxide is a mixture of Sb_2O_3 and Sb_2O_5 because the literature is unclear on the distinction between the two oxides in the spectra[42–45]. Nevertheless, this Sb-O species is drastically reduced on surface cleaning, showing that the oxide is present only at the surface of the sample and formed during atmospheric exposure. After cleaning, a small amount of oxide remained on the surface, which was not removed to avoid inducing sample damage through prolonged, excessive sputtering. It is also possible that this remnant oxide is present in the bulk

of the sample and so could not be removed by surface cleaning; however, due to the low level of oxide remaining (see Supporting Information for details), it is thought to have little effect on the measurements. The O 1s peak at higher binding energy (orange shading) is consistent with an adventitious species associated with carbon[46], while the peak at lower binding energy (purple shading) that almost fully overlaps the antimony oxide Sb $3d_{5/2}$ peak is attributed to the oxygen from within this antimony oxide[43], as it is also reduced upon cleaning. The third, small antimony doublet at lower binding energy (blue dot dash) is attributed to metallic antimony[42]. It is believed that the metallic antimony is not created by the preferential sputtering of sulfur, nor the dissociation of sulfur during the surface cleaning for several reasons. Firstly, the amount of metallic antimony relative to the antimony from CAS decreases after surface cleaning, whereas if it were created by the surface cleaning, one would expect it to increase. Secondly, surface cleaning-induced damage to the sample was minimized by using relatively low sputtering energies and anneal temperatures, as detailed in the experimental section. In a separate study where high energy sputtering was used (3 keV)[8,18], the amount of sputter-induced antimony was markedly higher and could have a significant effect on the measurements. Further discussion of the presence of metallic antimony is given in the Supporting Information.

Figure 5. XPS spectra for the Sb 3d and O 1s overlap region of the CAS sample before and after surface cleaning. Peak envelope shown in black.

A comparison of the S 2p spectra before and after surface cleaning is shown in Figure 6. Doublets were fitted with a separation of 1.18 eV[47] and an area ratio of 1:2. Before cleaning, the spectra were fit with three doublets, and after cleaning, were fit with two doublets. The species which was eliminated after cleaning (green shading) is attributed to sulfur-containing surface contamination[48], as seen in other sulfide materials[32]. The two strongest doublets (red dash & blue dot), separated by 0.3 eV are assigned to S^{2-} in CAS. Each doublet is attributed to one of the two different sulfur coordination sites described in the introduction (see Figure 1). In the literature, few attempts at fitting the S 2p region have been made, and only one group fit it with more than one doublet[8,18]; however, the signal-to-noise ratio (SNR) is poor and the authors state that the extra doublets are due to unreacted precursor. It is our opinion, however, that the extra sulfur peaks in that study were probably due to sputter damage, affirmed by the sputter profile shown there. The viability of the presence of two doublets in Figure 6 is initially confirmed by the poor quality of fit when using one doublet (see Figure S2), and is strengthened by: the area ratio between the doublets being 1:1, as expected from the crystal structure; samples previously measured by the authors being fit this way equally well[33]; and the large difference in coordination environments for the sulfur. Despite this, the specific assignment of the S 2p doublets to their corresponding coordination environment is unclear, because of the severely distorted structure of CAS and the complications involved with predicting the binding energies of sulfur for complex systems[49]. Also, although the S1 environment is coordinated to an extra cation, two of the bonds with antimony are significantly longer (3.12 Å) than the others[28] (2.30 – 2.57 Å), and as such are believed to be governed by van der Waals forces[50]. Therefore, the

amount of charge transfer, differences in electronegativities of the cations, the effect of bond lengths and second-nearest neighbors will all contribute differently to the binding energy, and as such, no definitive assignment is given here. Prior to cleaning, the sample showed no presence of sulfate species, as has been seen in previous reports of this material[22,33].
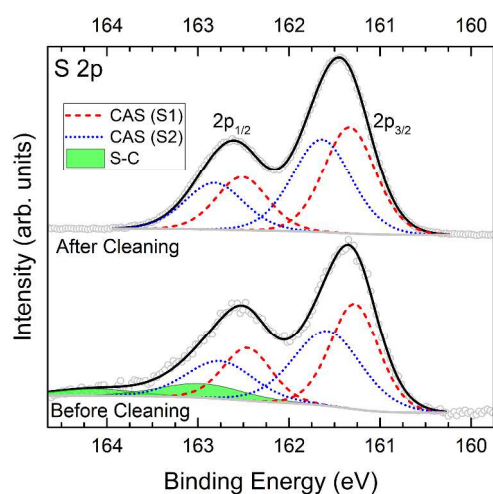

Figure 6. XPS spectra for the S 2p region of the CAS sample before and after surface cleaning. Peak envelope shown in black.

Generally, the binding energies reported for this material are in poor agreement with those measured here, excepting one study with well fitted data[2], and other CAS samples measured by the authors[33]. However, it is believed that some studies are lacking a charge correction[17], or have misapplied one[23], as the relative binding energy differences are in agreement with those measured here. Furthermore, other studies which are in contrast with our values suffer as their binding energies were either not quoted[22], not fitted in the case of multi-component regions[21], or the SNR were so poor that no values could be confidently assigned[20]. The merit of these analyses therefore cannot be evaluated. Additionally, as discussed above, the presence of contamination and oxide formation can affect the measured binding energies and band positions, which can also

change as a function of composition and by the presence of mixed phases. In this respect, some studies seem to suffer from this without full acknowledgement of the ramifications[8,13,18].

As shown in Table 1, the shifts in binding energy before and after surface cleaning are rather small and so it is concluded that the gentle cleaning employed here did not significantly affect the underlying material. Further discussion on the binding energies, including those from contamination, can be found in the Supporting Information, along with all fitted binding energies in Table S1. Also presented in the Supporting Information are the XPS-derived surface stoichiometry values, and a discussion and comparison of the electronic structure and sample quality of the as-deposited and annealed material.

Table 1. XPS binding energies[a] determined for the main peaks of CAS and electronic band positions[b] before and after surface cleaning[c].

Sample	$CuSbS_2$						
	Cu $2p_{3/2}$	Sb $3d_{5/2}$	S $2p_{3/2}$ (1)	S $2p_{3/2}$ (2)	WF	IP	EA
Before Cleaning	931.97 (1.13)	529.11 (0.80)	161.28 (0.62)	161.58 (0.88)			
After Cleaning	931.97 (1.13)	529.19 (0.86)	161.33 (0.66)	161.64 (0.76)	4.73	4.98	3.43

[a] Peak FWHM are given in parentheses and the binding energies of all fitted peaks in this study can be found in Table S1.

[b] Values of: work function (WF), ionization potential (IP), and electron affinity (EA) were calculated from XPS and optical absorption spectra.

[c] All values are given in eV.

Band Edge Positions. When considering solar cell materials, an often overlooked point to consider is how the band edge positions affect the architecture of the cell. Whilst a desirable absorber band gap is necessary for decent efficiencies, performance is largely compromised if the band alignments hinder charge carrier extraction.

Nevertheless, the direct and indirect band gaps of $CuSbS_2$ were determined from the absorption spectra both at room and cryogenic temperatures using the method described in the literature[51], and are shown in the Tauc plots in Figure 7. Room temperature measurements (300 K) allow the extraction of both the direct (1.60 eV) and indirect (1.55 eV) band gaps, which are in agreement with a previous study that found the direct transition to lie 0.1 eV higher than the indirect transition, and led to previous misclassification of the fundamental gap of this material to be direct in nature[7]. The direct and indirect gaps at cryogenic temperatures (4 K) were also determined for comparison with the DFT calculations and were found to be 1.69 eV and 1.59 eV respectively. As the DFT HSE06 (0 K) direct and indirect band gaps were found to be 1.82 eV and 1.67 eV respectively, this is in satisfactory agreement with the experimental results at 4 K, with the slight discrepancy explained because of the lack of inclusion of excitonic effects which may affect the experimental absorption.
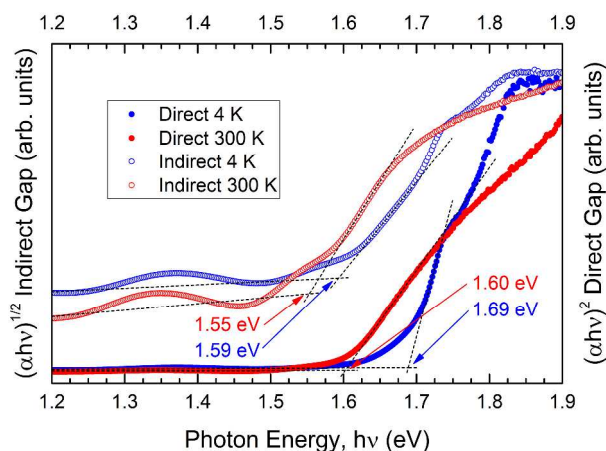

Figure 7. Optical absorption data from CAS. Tauc plot fittings for the direct and indirect gaps of the CAS sample at 4 K and 300 K.

It is also important, at least from an initial cell-design perspective, that the relative energies between the conduction band minimum (CBM) and valence band maximum (VBM) are known with respect to the vacuum level: these are the electron affinity (EA) and ionization potential (IP)

respectively. Direct measurements of IP are possible using XPS, the method of which is described elsewhere[32]. The IP and, as a consequence work function (WF), of CAS after cleaning were determined to be 4.98 eV and 4.73 eV respectively from the fittings shown in Figure S8. By using a vacuum alignment procedure[52] and taking the measured indirect and direct 300 K band gap value of 1.55 eV and 1.60 eV from Figure 7 respectively, the band alignment is compared with CZTS, CIGS and CdS in Figure 8, with the values of IP and WF shown in Table 1 (literature values of ionization potential and band gap are taken for CdS[53], CIGS[54] and CZTS[53]). An EA of 3.43 eV was determined from the difference between the measured IP and indirect band gap.
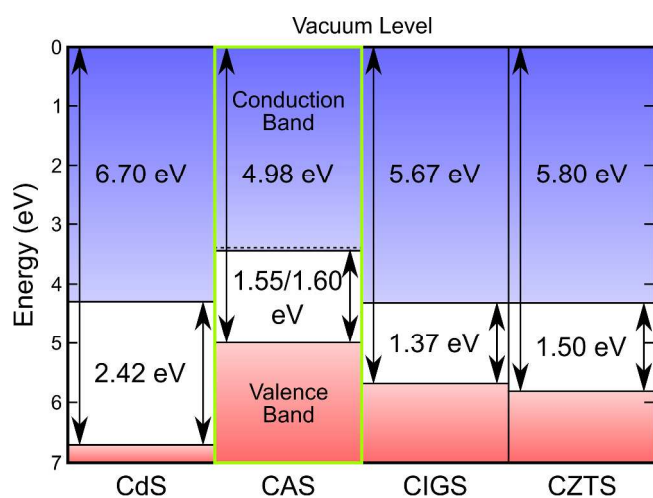
Figure 8. Vacuum-aligned band diagram for CAS derived from XPS IP and optical indirect (solid line) and direct (dashed line) band gap measurements compared with other common absorbers and the common n-type window layer material, CdS.

Although XPS can be used to great effect in determining band positions[55] and also performing band alignments at junction interfaces[56], it is not widely performed, especially on new materials. Hence these measurements are absent from the majority of CAS literature. However, one study[13] using ultraviolet photoemission spectroscopy (UPS) measured a WF of 4.86 eV, in good

agreement with our values, and an ionization potential of 5.25 eV, which considering the apparent level of contamination present in this cited study, is not unexpected as the fitting for the VBM is unclear. In another study, with extremely heavy antimony oxide contamination present, a very high IP and band gap (2.75 eV) were measured[33]. This suggests that the presence of antimony oxide could be a contributing factor to the poor performance of CAS so far, because Sb_2O_3 has a relatively large band gap[57] and would act as an insulating layer within the cell. It is proposed that only with the use of surface sensitive techniques such as XPS, that the true ramifications of this oxide formation can be determined, because as the oxide is very thin (<3nm, evidenced from the spectral ratios and estimated escape depth of electrons in Figure S6), optical measurements of the band gap would not be affected by it. Also, as the oxide crystallinity is probably poor and given the thinness of this layer, identification may be missed by XRD analysis. In this respect, surface sensitive XPS can provide indispensable information: identifying unwanted contaminants and also measuring the effect they have on the electronic structure.

It has been previously suggested that the poor open circuit voltage (V_{OC}) in CAS cells arises partly from a poor conduction band (CB) alignment with the n-type layer[4], and this is confirmed here in Figure 8, with the conduction band of CAS lying 0.85 eV higher than that of CdS, which with such a high conduction band offset (CBO), would suggest that a recombination center would be present here[58]. In fact, in order to stop the formation of an electron barrier at the interface, the conduction band of the n-type layer should be 0–0.4 eV higher than that of the absorber[59], as is the case with both CIGS/CdS and CZTS/CdS as seen in Figure 8. It is therefore obvious that utilizing traditional CIGS cell architectures for CAS is unfavorable for device performance. The use of CdS as the n-type layer not only creates the cliff-like CBO[4], but also

undermines the goal of developing environmentally-friendly structures. It may also be the case that along with replacing the n-type layer, the back contact may also need replacing as the work function of typically-used molybdenum (4.35–4.90 eV[60]) may not be favorable for charge extraction. It is therefore apparent that further research is needed to identify more ideal partner materials for CAS in a cell; this could be achieved by measuring the band alignments of grown heterojucntions.

Density of States. The IP found in the previous section is unusually low compared with other PV absorbers (see Figure 8). This has been seen previously in materials with non-bonding lone pairs[32], where this electronic structure feature was the reason for the remarkably high bands, causing a CB misalignment with CdS, and it is thought that a similar situation could be present in CAS as well. The partial density of states (pDoS) in the valence band along with the experimentally measured valence band spectra from XPS (after cleaning) are shown in Figure 9. A Shirley background was subtracted from the spectra to account for inelastically scattered electrons. The pDoS curves were corrected using standard photoionisation cross sections[61], convolved with a Gaussian function (0.38 eV FWHM) to account for thermal broadening and the spectrometer resolution, and then further convolved with a Lorentzian function (0.25 eV FWHM) to account for lifetime broadening. The corrected pDoS curves were then summed, and the total curve aligned to the XPS data for direct comparison. There is generally good agreement between the calculated density of states (DoS) and the XPS spectra, with all features accounted for and the relative intensities of the correct order. Especially, Cu 3d states of the main feature (II) and the leading edge at the top of the valence band (I) are reproduced well. The only differences arise at features III and IV (better shown in the zoomed region of Figure 9), probably

due to final-state relaxation effects in XPS, which are known to shift features which are deeper in the valence band to lower binding energies[32].
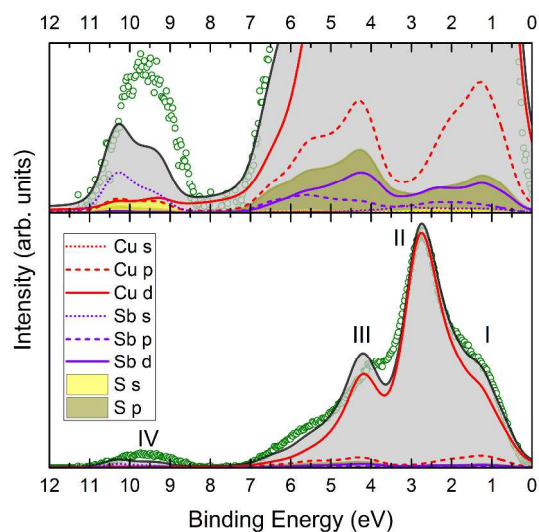
Figure 9. Simulated and measured VB spectra for CAS with respect to the Fermi level at 0 eV. Background subtracted XPS data is compared with broadened and corrected partial DoS curves. Top spectra shows intensity zoomed region to better show the underlying curves. Green data are from XPS and black curve with grey shading is the total summed DoS.

Following the excellent experimental corroboration from comparing XPS spectra and corrected DoS curves, it is now prudent to discuss the pDoS contributions with respect to the uncorrected curves due to the dominance of Cu 3d states arising from the large photoionisation cross section of this orbital. Thus, these are shown in Figure 10a, also with the corresponding DoS for the CB. Without the corrections, the VBDoS is still dominated by Cu 3d states, and the valence band shows three distinct features (V, VI & V*). Similar to both CIGS and CZTS, the copper in CAS is tetrahedrally coordinated to sulfur in the crystal structure and therefore the crystal field splits the Cu 3d orbitals into a non-bonding e doublet, and a t_2 triplet, which is able to bond[62]. These features are present in Figure 10 as the non-bonding e_g states (VI), and the bonding (V) and antibonding (V*) hybridization of the t_{2g} states with S 3p states. The bottom of the highest

valence band is comprised of bonding orbitals of S 3p states with a slight contribution from Sb

5p states (VII), and the antibonding states of this interaction form the main contribution to the
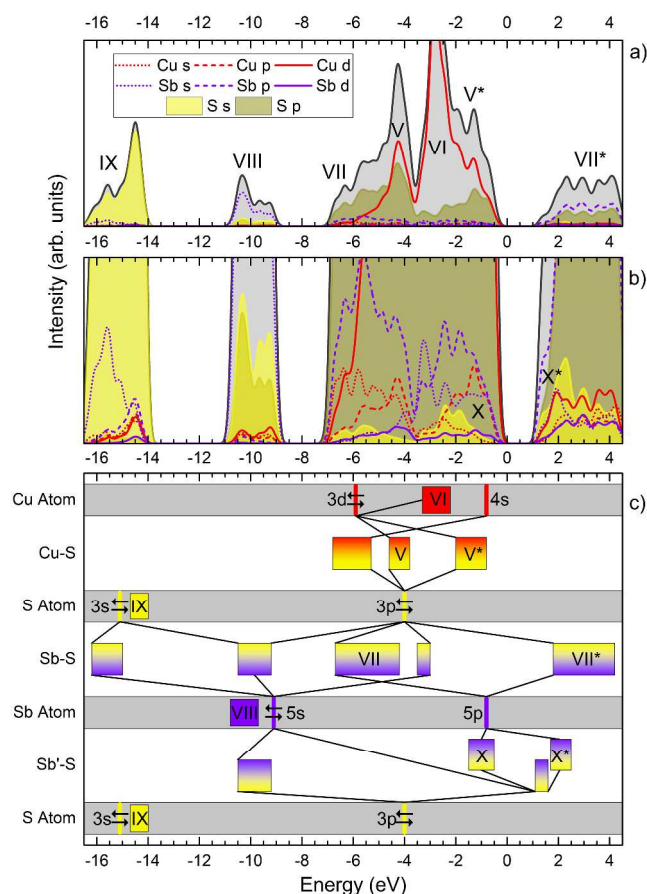
conduction band (VII*).

Figure 10. a) & b) Total and partial electronic density of states curves for CAS, with intensity

zoomed region to more clearly show the underlying orbitals. Curves have been convolved with a

Gaussian function (0.3 eV FWHM) in order to better distinguish features. DoS curves are aligned

to the VBM. Black curve with grey shading is the total summed DoS. c) Configuration energies

for the valence orbitals displayed with a schematic of the bonding hybridizations as discussed in

the text. It is noted that these values do not take ionization, multi-electron occupancy or

hybridization into account and are shown only as a schematic guide. Part labels are discussed and

referred to throughout the text.

Further insights into the bonding nature are gained when studying the states normally overwhelmed by intensity from Cu d/S p hybridization and to this end, we consider the zoomed region of the valence and conduction band edges in Figure 10b. At first glance, it would seem that the Sb 5s states are localized at ~10 eV in feature VIII, which agrees with the classical model of lone pair electrons: that they are too tightly bound and therefore non-bonding. However, there are also Sb s states at the top of the valence band (X) and the bottom of the conduction band (X*), which suggests that the contribution here is due to interactions via the revised lone pair model[29]. In this model, the lone pair electrons firstly interact with S 3p electrons and the full antibonding orbital of this interaction is then sufficiently high so that it can subsequently interact with empty Sb 5p states, resulting in bonding states in the valence band (X) and antibonding states at the bottom of the conduction band (X*). Our findings, in agreement with previous analyses of the VBDoS of CAS[1,30], are in direct opposition to a more recent study which claimed that the Sb 5s lone pair is inert, localized and contributes nothing to bonding in the valence band[27]. We believe this interpretation to be incorrect for two main reasons: first, because the top of the valence band is so well reproduced between the DoS and XPS spectrum, our bonding model is supported, even though the Sb states have weak cross sections when compared to the Cu states. Second, due to the distorted nature of the SbS_5 pyramids in the crystal structure, the revised lone pair model suggests that these interactions should indeed take place. In fact, the structure is stabilized by projecting states into the crystal void, whereas in undistorted structures, this interaction is symmetry forbidden[30].

The bonding mechanisms described above and the other main contributions are shown schematically in Figure 10c to more clearly demonstrate the proposed hybridizations from the

configuration energies (CE)[63,64], most importantly, the effect of the lone pairs and the nature of the Cu 3d states in the valence band.

The described features are in agreement with previous analyses of CAS DoS calculations[1,7,27,30]; however, no solid link has been previously made to the effect of these features regarding the electronic properties. As discussed previously, much initial progress was made likening CAS to CIGS and also to CZTS, and the comparisons are still drawn in analyses of the DoS[30], especially regarding the Cu 3d/S 3p states in the valence band[7], which are indeed very similar to the tetrahedral environment also present in CIGS. However, the full merit of this practice is questioned when it is clear that the crystal structure of CAS is so different from CIGS, then so should be the DoS as the bonding is what leads to the adopted crystal structure. Clearly, from the CBDoS, Sb 5p states are the main cation contributor in CAS, whereas in CIGS, the bottom of the CB is mainly In/Ga s states[62,65]. Consequently, this has been recognized previously and found to be the reason why CAS shows superior absorption to CIGS[66], but no further discussions have been made[27]. We then posit that this difference is also the cause of the low IP found previously and discussed above. In CIGS, the In/Ga are in the 3+ oxidation state, as is Sb in CAS, however, being group III elements, In/Ga have formally empty valence s orbitals for the 3+ oxidation state ($[Kr]4d^{10}5s^{0}5p^{0}$/$[Ar]3d^{10}4s^{0}4p^{0}$), whereas in group V Sb, it is full ($[Kr]4d^{10}5s^{2}5p^{0}$). This means that in CIGS, empty cation s orbitals bond with full anion p orbitals to form regular full bonding states at the bottom of the valence band and empty antibonding states at the bottom of the conduction band, whereas in CAS the full Sb 5s orbital is available for bonding and due to the mechanism described above, states are found throughout the valence band and at the bottom of the conduction band. It is unsurprising that the first conduction band of CAS is dominated by antibonding Sb 5p/S 3p states as Sb-5p are the first empty orbitals that are

energetically within the proximity of the full S 3p orbitals. This is shown, in contrast to the

empty states of CIGS, in the schematic configuration energy[63,64] diagram in Figure 11, with the

main contributions to the VBM and CBM marked. From this, we can also see that the empty

cation s states in CIGS are energetically closer to the anion p orbital than the also empty cation p

orbitals, and therefore the cation s nature of the CBM in CIGS is explained as well.
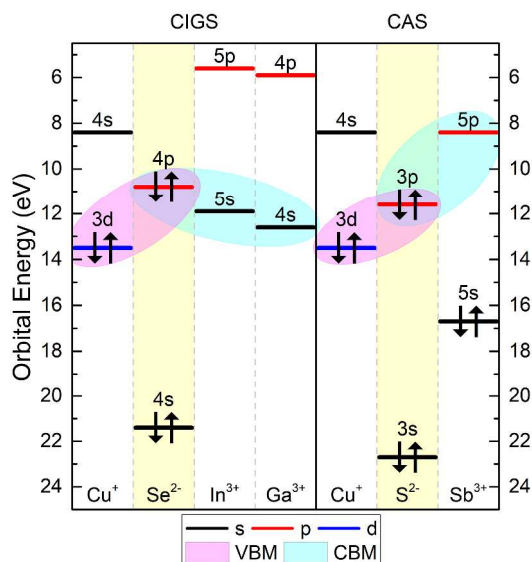

Figure 11. Configuration energies for the valence orbitals of CIGS and CAS. The formal ionic

occupancy of the orbitals within the materials are marked and the main orbital contributions to

the VBM and CBM are shown.

Although we believe that the Sb lone pair plays some part in raising the energy levels of the

bands in CAS, the Cu d states must also have an effect due to their dominating presence in the

valence band. In other dominant d-orbital semiconductors, the chemical trend is that with

increasing separation between the cation d and anion p levels, the VBM position rises, given a

common-cation[67]. If one accepts this, then by studying Figure 11, the CAS analogue replacing S

with Se, that is $CuSbSe_2$ (CASe), should yield a lower IP than CAS, and this has been previously

reported[1,68]. This then, would suggest that CIGS, with common Cu-cation, and Se as an anion,

should show a similar trend when compared to CAS. As this is not the case, it is then evident that it is the presence of antimony over indium/gallium which is responsible for the elevation of the valence band, both through the addition of Sb 5s states to the valence band, but also the shifting of Cu 3d states within the VBM.

As has been shown before, the growth method can strongly affect the device quality with regards to contaminant formation. However, another issue is the formation of defects within the absorber material which can also affect device performance. 'Defect tolerance' is a term used when the formation of defects does not negatively affect the properties of a material and has been classified to occur when the VBM is antibonding in nature and the CBM is bonding in nature, so that defects would produce only shallow levels[69]. To this extent, CAS should benefit from at least some measure of this property because even though the CBM is predominantly antibonding Sb p/S p states, the VBM is strongly antibonding Cu d/S p with also a slight contribution from Sb s states due to the lone pair bonding mechanism. Furthermore, the dominant vacancy in CAS has been shown to be the acceptor copper vacancy (V_{Cu})[13] which leads to the inherent p-type conductivity and also the crystallographic differences between the two cation-anion environments makes CAS less prone to cation disorder, and the band tailing associated with it[3], both of which support the idea that CAS should be defect tolerant.

These observations and reasoning all support the postulate that advancement in CAS research now requires a definitive move away from CIGS analogies. The lone pair of electrons from the antimony cation provides extra states to both the valence and conduction bands of CAS, which are not present in CIGS. This leads to a higher VBM level, resulting in a markedly low IP for CAS, which results in a performance-damaging CBO with CdS. Therefore, CAS should be

developed, along with its true analogous materials (the [Cu-(Sb/Bi)-(S/Se)] family of systems), as its own class of earth-abundant absorber materials.

CONCLUSIONS

The valence band density of states and the size and nature of the band gaps of the promising absorber material, $CuSbS_2$ have been compared experimentally and theoretically for the first time. We show that the strong Cu d nature of the valence band obscures states arising from the antimony, but which play a role in determining the properties of the material. In contrast with CIGS, the conduction band minimum consists of non-copper cation p/anion p states rather than non-copper cation s/anion p states as in CIGS; a result of Sb^{3+} being a group V element rather than the group III $(In/Ga)^{3+}$ in CIGS. The full Sb 5s states therefore also feature at the top of the valence band through the revised lone pair model, along with Sb 5p states. These extra contributions to the valence band play some role in raising the VBM and causing the low IP of 4.98 eV observed here. The band levels measured here support the reasoning that CdS is an inappropriate n-type window layer for CAS because of the large CBO, resulting from the low EA (3.43 eV) which was determined using a combination of IP measurements from XPS and a band gap measurement of 1.55 eV from the room temperature indirect absorption spectra. This approach to cell design, which arises from CIGS development, is part of the reason that CAS has seen poor performance. We have also shown a thorough core-level XPS analysis of CAS, which reveals that the two sulfur coordination environments can be determined by XPS, and also the effects of contamination, which is crucial given the spectral complexities of this material. Following a thorough literature survey of this material, it is believed that these complexities have led to misinterpretations of XPS spectra, and therefore this could have also contributed to the poor performance of CAS cells. It is therefore clear that the use of CdS as the n-type layer in

CAS cells is less favorable than for CIGS cells. However, with alternative n-type material with better band alignments, the potential of CAS as a solar absorber remains.

ASSOCIATED CONTENT

Supporting Information.

The following files are available free of charge.

Explanation of the XPS fitting procedure used throughout this study, discussion of the effects of sodium detected in the samples (Figure S1), justification of fitting two S 2p doublets to CAS (Figure S2), a comparison between the effect of the thermal treatment on the XPS spectra (Figure S3–S8), all of the fitted XPS binding energies in this study (Table S1), surface stoichiometry values from XPS (Table S2) (PDF)

AUTHOR INFORMATION

Corresponding Author

*E-mail: vin@liverpool.ac.uk

Notes

The authors declare no competing financial interest.

REFERENCES

(1)   Temple, D. J.; Kehoe, A. B.; Allen, J. P.; Watson, G. W.; Scanlon, D. O. Geometry, Electronic Structure, and Bonding in $CuMCh_2$ (M = Sb, Bi; Ch = S, Se): Alternative Solar Cell Absorber Materials? *J. Phys. Chem. C* **2012**, *116* (13), 7334–7340.

(2)   Wan, L.; Ma, C.; Hu, K.; Zhou, R.; Mao, X.; Pan, S.; Wong, L. H.; Xu, J. Two-Stage Co-Evaporated $CuSbS_2$ Thin Films for Solar Cells. *J. Alloys Compd.* **2016**, *680*, 182–190.

(3)   de Souza Lucas, F. W.; Welch, A. W.; Baranowski, L. L.; Dippo, P. C.; Hempel, H.; Unold, T.; Eichberger, R.; Blank, B.; Rau, U.; Mascaro, L. H.; Zakutayev, A. Effects of Thermochemical Treatment on $CuSbS_2$ Photovoltaic Absorber Quality and Solar Cell Reproducibility. *J. Phys. Chem. C* **2016**, *120* (33), 18377–18385.

(4)   Welch, A. W.; Baranowski, L. L.; Zawadzki, P.; DeHart, C.; Johnston, S.; Lany, S.; Wolden, C. A.; Zakutayev, A. Accelerated Development of $CuSbS_2$ Thin Film Photovoltaic Device Prototypes. *Prog. Photovoltaics Res. Appl.* **2016**, *24* (7), 929–939.

(5)   Rodríguez-Lazcano, Y.; Nair, M. T. S.; Nair, P. K. $CuSbS_2$ Thin Film Formed through Annealing Chemically Deposited Sb_2S_3–CuS Thin Films. *J. Cryst. Growth* **2001**, *223* (3), 399–406.

(6)   Kehoe, A. B.; Temple, D. J.; Watson, G. W.; Scanlon, D. O. Cu_3MCh_3 (M = Sb, Bi; Ch = S, Se) as Candidate Solar Cell Absorbers: Insights from Theory. *Phys. Chem. Chem. Phys.* **2013**, *15* (37), 15477.

(7)   Kumar, M.; Persson, C. $CuSbS_2$ and $CuBiS_2$ as Potential Absorber Materials for Thin-Film Solar Cells. *J. Renew. Sustain. Energy* **2013**, *5* (3), 31616.

(8)   Ornelas-Acosta, R. E.; Shaji, S.; Avellaneda, D.; Castillo, G. a.; Das Roy, T. K.; Krishnan, B. Thin Films of Copper Antimony Sulfide: A Photovoltaic Absorber Material. *Mater. Res. Bull.* **2015**, *61*, 215–225.

(9)   Rodríguez-Lazcano, Y.; Nair, M. T. S.; Nair, P. K. Photovoltaic P-I-N Structure of Sb_2S_3 and $CuSbS_2$ Absorber Films Obtained via Chemical Bath Deposition. *J. Electrochem. Soc.* **2005**, *152* (8), G635–G638.

(10) Garza, C.; Shaji, S.; Arato, A.; Perez Tijerina, E.; Alan Castillo, G.; Das Roy, T. K.; Krishnan, B. P-Type $CuSbS_2$ Thin Films by Thermal Diffusion of Copper into Sb_2S_3. *Sol. Energy Mater. Sol. Cells* **2011**, *95* (8), 2001–2005.

(11) Septina, W.; Ikeda, S.; Iga, Y.; Harada, T.; Matsumura, M. Thin Film Solar Cell Based on $CuSbS_2$ Absorber Fabricated from an Electrochemically Deposited Metal Stack. *Thin Solid Films* **2014**, *550*, 700–704.

(12) Popovici, I.; Duta, A. Tailoring the Composition and Properties of Sprayed $CuSbS_2$ Thin Films by Using Polymeric Additives. *Int. J. Photoenergy* **2012**, *2012*, 1–6.

(13) Yang, B.; Wang, L.; Han, J.; Zhou, Y.; Song, H.; Chen, S.; Zhong, J.; Lv, L.; Niu, D.; Tang, J. $CuSbS_2$ as a Promising Earth-Abundant Photovoltaic Absorber Material: A Combined Theoretical and Experimental Study. *Chem. Mater.* **2014**, *26* (10), 3135–3143.

(14) Colombara, D.; Peter, L. M.; Rogers, K. D.; Painter, J. D.; Roncallo, S. Formation of $CuSbS_2$ and $CuSbSe_2$ Thin Films via Chalcogenisation of Sb–Cu Metal Precursors. *Thin Solid Films* **2011**, *519* (21), 7438–7443.

(15) Krishnan, B.; Shaji, S.; Ernesto Ornelas, R. Progress in Development of Copper Antimony Sulfide Thin Films as an Alternative Material for Solar Energy Harvesting. *J. Mater. Sci. Mater. Electron.* **2015**, *26* (7), 4770–4781.

(16) Welch, A. W.; Zawadzki, P. P.; Lany, S.; Wolden, C. A.; Zakutayev, A. Self-Regulated Growth and Tunable Properties of $CuSbS_2$ Solar Absorbers. *Sol. Energy Mater. Sol. Cells* **2015**, *132*, 499–506.

(17) Ramos Aquino, J. A.; Rodriguez Vela, D. L.; Shaji, S.; Avellaneda, D. A.; Krishnan, B. Spray Pyrolysed Thin Films of Copper Antimony Sulfide as Photovoltaic Absorber. *Phys. status solidi* **2016**, *13* (1), 24–29.

(18) Ornelas-Acosta, R. E.; Avellaneda, D.; Shaji, S.; Castillo, G. a.; Das Roy, T. K.; Krishnan, B. CuSbS$_2$ Thin Films by Heating Sb$_2$S$_3$/Cu Layers for PV Applications. *J. Mater. Sci. Mater. Electron.* **2014**, *25* (10), 4356–4362.

(19) Suehiro, S.; Horita, K.; Yuasa, M.; Tanaka, T.; Fujita, K.; Ishiwata, Y.; Shimanoe, K.; Kida, T. Synthesis of Copper–Antimony-Sulfide Nanocrystals for Solution-Processed Solar Cells. *Inorg. Chem.* **2015**, *54* (16), 7840–7845.

(20) An, C.; Liu, Q.; Tang, K.; Yang, Q.; Chen, X.; Liu, J.; Qian, Y. The Influences of Surfactant Concentration on the Quality of Chalcostibite Nanorods. *J. Cryst. Growth* **2003**, *256* (1–2), 128–133.

(21) Suriakarthick, R.; Nirmal Kumar, V.; Shyju, T. S.; Gopalakrishnan, R. Effect of Substrate Temperature on Copper Antimony Sulphide Thin Films from Thermal Evaporation. *J. Alloys Compd.* **2015**, *651*, 423–433.

(22) Su, H.; Xie, Y.; Wan, S.; Li, B.; Qian, Y. A Novel One-Step Solvothermal Route to Nanocrystalline CuSbS$_2$ and Ag$_3$SbS$_3$. *Solid State Ionics* **1999**, *123* (1–4), 319–324.

(23) Ramasamy, K.; Gupta, R. K.; Sims, H.; Palchoudhury, S.; Ivanov, S.; Gupta, A. Layered Ternary Sulfide CuSbS$_2$ Nanoplates for Flexible Solid-State Supercapacitors. *J. Mater. Chem. A* **2015**, *3* (25), 13263–13274.

(24) Choi, Y. C.; Yeom, E. J.; Ahn, T. K.; Seok, S. Il. CuSbS$_2$ -Sensitized Inorganic-Organic Heterojunction Solar Cells Fabricated Using a Metal-Thiourea Complex Solution. *Angew. Chemie Int. Ed.* **2015**, *54* (13), 4005–4009.

(25) Marino, C.; Block, T.; Pöttgen, R.; Villevieille, C. CuSbS$_2$ as a Negative Electrode Material for Sodium Ion Batteries. *J. Power Sources* **2017**, *342*, 616–622.

(26) Banu, S.; Ahn, S. J.; Ahn, S. K.; Yoon, K.; Cho, A. Fabrication and Characterization of Cost-Efficient CuSbS$_2$ Thin Film Solar Cells Using Hybrid Inks. *Sol. Energy Mater. Sol. Cells* **2016**, *151*, 14–23.

(27) Maeda, T.; Wada, T. First-Principles Study of Electronic Structure of CuSbS$_2$ and CuSbSe$_2$ Photovoltaic Semiconductors. *Thin Solid Films* **2015**, *582*, 401–407.

(28) Kyono, A. Crystal Structures of Chalcostibite (CuSbS$_2$) and Emplectite (CuBiS$_2$): Structural Relationship of Stereochemical Activity between Chalcostibite and Emplectite. *Am. Mineral.* **2005**, *90* (1), 162–165.

(29) Walsh, A.; Payne, D. J.; Egdell, R. G.; Watson, G. W. Stereochemistry of Post-Transition Metal Oxides: Revision of the Classical Lone Pair Model. *Chem. Soc. Rev.* **2011**, *40* (9), 4455–4463.

(30) Dufton, J. T. R.; Walsh, A.; Panchmatia, P. M.; Peter, L. M.; Colombara, D.; Islam, M. S. Structural and Electronic Properties of CuSbS$_2$ and CuBiS$_2$: Potential Absorber Materials for Thin-Film Solar Cells. *Phys. Chem. Chem. Phys.* **2012**, *14* (20), 7229.

(31) Birkett, M.; Savory, C. N.; Fioretti, A. N.; Thompson, P.; Muryn, C. A.; Weerakkody, A. D.; Mitrovic, I. Z.; Hall, S.; Treharne, R.; Dhanak, V. R.; Scanlon, D. O.; Zakutayev, A.; Veal, T. D. Atypically Small Temperature-Dependence of the Direct Band Gap in the Metastable Semiconductor Copper Nitride Cu$_3$N. *Phys. Rev. B* **2017**, *95* (11), 115201.

(32)　Whittles, T. J.; Burton, L. A.; Skelton, J. M.; Walsh, A.; Veal, T. D.; Dhanak, V. R. Band Alignments, Valence Bands, and Core Levels in the Tin Sulfides SnS, SnS_2 , and Sn_2S_3: Experiment and Theory. *Chem. Mater.* **2016**, *28* (11), 3718–3726.

(33)　Peccerillo, E.; Major, J.; Phillips, L.; Treharne, R.; Whittles, T. J.; Dhanak, V.; Halliday, D.; Durose, K. Characterization of Sulfurized $CuSbS_2$ Thin Films for PV Applications. In *2014 IEEE 40th Photovoltaic Specialist Conference (PVSC)*; IEEE, 2014; pp 0266–0269.

(34)　Rath, T.; MacLachlan, A. J.; Brown, M. D.; Haque, S. A. Structural, Optical and Charge Generation Properties of Chalcostibite and Tetrahedrite Copper Antimony Sulfide Thin Films Prepared from Metal Xanthates. *J. Mater. Chem. A* **2015**, *3* (47), 24155–24162.

(35)　Efthimiopoulos, I.; Buchan, C.; Wang, Y. Structural Properties of Sb_2S_3 under Pressure: Evidence of an Electronic Topological Transition. *Sci. Rep.* **2016**, *6* (April), 24246.

(36)　Mernagh, T. P.; Trudu, A. G. A Laser Raman Microprobe Study of Some Geologically Important Sulphide Minerals. *Chem. Geol.* **1993**, *103* (1–4), 113–127.

(37)　Qiu, X. D.; Ji, S. L.; Chen, C.; Liu, G. Q.; Ye, C. H. Synthesis, Characterization, and Surface-Enhanced Raman Scattering of near Infrared Absorbing Cu_3SbS_3 Nanocrystals. *Crystengcomm* **2013**, *15* (48), 10431.

(38)　Aup-Ngoen, K.; Thongtem, T.; Thongtem, S. Characterization of Cu_3SbS_4 Microflowers Produced by a Cyclic Microwave Radiation. *Mater. Lett.* **2012**, *66* (1), 182–186.

(39)　Lebugle, A.; Axelsson, U.; Nyholm, R.; Mårtensson, N. Experimental L and M Core Level Binding Energies for the Metals 22 Ti to 30 Zn. *Phys. Scr.* **1981**, *23* (5A), 825–827.

(40) Nyholm, R.; Martensson, N.; Lebugle, A.; Axelsson, U. Auger and Coster-Kronig Broadening Effects in the 2p and 3p Photoelectron Spectra from the Metals 22 Ti- 30 Zn. *J. Phys. F Met. Phys.* **1981**, *11* (8), 1727–1733.

(41) Delobel, R.; Baussart, H.; Leroy, J.-M.; Grimblot, J.; Gengembre, L. X-Ray Photoelectron Spectroscopy Study of Uranium and Antimony Mixed Metal-Oxide Catalysts. *J. Chem. Soc. Faraday Trans. 1 Phys. Chem. Condens. Phases* **1983**, *79* (4), 879.

(42) Morgan, W. E.; Stec, W. J.; van Wazer, J. R. Inner-Orbital Binding Energy Shifts of Antimony and Bismuth Compounds. *Inorg. Chem.* **1972**, *12* (4), 953–955.

(43) Garbassi, F. XPS and AES Study of Antimony Oxides. *Surf. Interface Anal.* **1980**, *2* (5), 165–169.

(44) Tang, X.; Welzenis, R. G. van; Setten, F. M. van; Bosch, A. J. Oxidation of the InSb Surface at Room Temperature. *Semicond. Sci. Technol.* **1986**, *1* (6), 355–365.

(45) Petit, E. J.; Riga, J.; Caudano, R. Surface and Interface XPS Characterization of the Oxide Layer Grown on Antimony under UV Laser Irradiation. *Surf. Sci.* **1991**, *251–252*, 529–534.

(46) Payne, B. P.; Biesinger, M. C.; McIntyre, N. S. X-Ray Photoelectron Spectroscopy Studies of Reactions on Chromium Metal and Chromium Oxide Surfaces. *J. Electron Spectros. Relat. Phenomena* **2011**, *184* (1–2), 29–37.

(47) Barrie, A.; Drummond, I. W.; Herd, Q. C. Correlation of Calculated and Measured 2p Spin-Orbit Splitting by Electron Spectroscopy Using Monochromatic X-Radiation. *J. Electron Spectros. Relat. Phenomena* **1974**, *5* (1), 217–225.

(48) Lindberg, B. J.; Hamrin, K.; Johansson, G.; Gelius, U.; Fahlman, A.; Nordling, C.; Siegbahn, K. Molecular Spectroscopy by Means of ESCA II. Sulfur Compounds. Correlation of Electron Binding Energy with Structure. *Phys. Scr.* **1970**, *1* (5–6), 286–298.

(49) Gerson, A. R.; Bredow, T. Interpretation of Sulphur 2p XPS Spectra in Sulfide Minerals by Means of Ab Initio Calculations. *Surf. Interface Anal.* **2000**, *29* (2), 145–150.

(50) Ramasamy, K.; Sims, H.; Butler, W. H.; Gupta, A. Selective Nanocrystal Synthesis and Calculated Electronic Structure of All Four Phases of Copper–Antimony–Sulfide. *Chem. Mater.* **2014**, *26* (9), 2891–2899.

(51) Viezbicke, B. D.; Patel, S.; Davis, B. E.; Birnie, D. P. Evaluation of the Tauc Method for Optical Absorption Edge Determination: ZnO Thin Films as a Model System. *Phys. status solidi* **2015**, *252* (8), 1700–1710.

(52) Klein, A. Energy Band Alignment in Chalcogenide Thin Film Solar Cells from Photoelectron Spectroscopy. *J. Phys. Condens. Matter* **2015**, *27* (13), 134201.

(53) Burton, L. A.; Walsh, A. Band Alignment in SnS Thin-Film Solar Cells: Possible Origin of the Low Conversion Efficiency. *Appl. Phys. Lett.* **2013**, *102* (13), 132111.

(54) Hinuma, Y.; Oba, F.; Kumagai, Y.; Tanaka, I. Ionization Potentials of (112) and ($11\bar{2}$) Facet Surfaces of $CuInSe_2$ and $CuGaSe_2$. *Phys. Rev. B* **2012**, *86* (24), 245433.

(55) Burton, L. A.; Whittles, T. J.; Hesp, D.; Linhart, W. M.; Skelton, J. M.; Hou, B.; Webster, R. F.; O'Dowd, G.; Reece, C.; Cherns, D.; Fermin, D. J.; Veal, T. D.; Dhanak, V. R.; Walsh, A. Electronic and Optical Properties of Single Crystal SnS_2: An Earth-Abundant Disulfide Photocatalyst. *J. Mater. Chem. A* **2016**, *4* (4), 1312–1318.

(56) Durose, K.; Asher, S. E.; Jaegermann, W.; Levi, D.; McCandless, B. E.; Metzger, W.; Moutinho, H.; Paulson, P. D.; Perkins, C. L.; Sites, J. R.; Teeter, G.; Terheggen, M. Physical Characterization of Thin-Film Solar Cells. *Prog. Photovoltaics* **2004**, *12* (2–3), 177–217.

(57) Allen, J. P.; Carey, J. J.; Walsh, A.; Scanlon, D. O.; Watson, G. W. Electronic Structures of Antimony Oxides. *J. Phys. Chem. C* **2013**, *117* (28), 14759–14769.

(58) Sinsermsuksakul, P.; Hartman, K.; Bok Kim, S.; Heo, J.; Sun, L.; Hejin Park, H.; Chakraborty, R.; Buonassisi, T.; Gordon, R. G. Enhancing the Efficiency of SnS Solar Cells via Band-Offset Engineering with a Zinc Oxysulfide Buffer Layer. *Appl. Phys. Lett.* **2013**, *102* (5), 53901.

(59) Minemoto, T.; Matsui, T.; Takakura, H.; Hamakawa, Y.; Negami, T.; Hashimoto, Y.; Uenoyama, T.; Kitagawa, M. Theoretical Analysis of the Effect of Conduction Band Offset of window/CIS Layers on Performance of CIS Solar Cells Using Device Simulation. *Sol. Energy Mater. Sol. Cells* **2001**, *67* (1–4), 83–88.

(60) Jacobson, D. L.; Campbell, A. E. Molybdenum Work Function Determined by Electron Emission Microscopy. *Metall. Mater. Trans. B* **1971**, *2* (11). 3063–3066.

(61) Yeh, J. J.; Lindau, I. Atomic Subshell Photoionization Cross Sections and Asymmetry Parameters: $1 \leqslant Z \leqslant 103$. *At. Data Nucl. Data Tables* **1985**, *32* (1), 1–155.

(62) Zhang, Y.; Yuan, X.; Sun, X.; Shih, B.-C.; Zhang, P.; Zhang, W. Comparative Study of Structural and Electronic Properties of Cu-Based Multinary Semiconductors. *Phys. Rev. B* **2011**, *84* (7), 75127.

(63) Mann, J. B.; Meek, T. L.; Allen, L. C. Configuration Energies of the Main Group Elements. *J. Am. Chem. Soc.* **2000**, *122* (12), 2780–2783.

(64) Mann, J. B.; Meek, T. L.; Knight, E. T.; Capitani, J. F.; Allen, L. C. Configuration Energies of the D-Block Elements. *J. Am. Chem. Soc.* **2000**, *122* (21), 5132–5137.

(65) Chen, X.-D.; Chen, L.; Sun, Q.-Q.; Zhou, P.; Zhang, D. W. Hybrid Density Functional Theory Study of $Cu(In_{1-x}Ga_x)Se_2$ Band Structure for Solar Cell Application. *AIP Adv.* **2014**, *4* (8), 87118.

(66) Yu, L.; Kokenyesi, R. S.; Keszler, D. A.; Zunger, A. Inverse Design of High Absorption Thin-Film Photovoltaic Materials. *Adv. Energy Mater.* **2013**, *3* (1), 43–48.

(67) Wei, S. H.; Zunger, A. Calculated Natural Band Offsets of All II-VI and III-V Semiconductors: Chemical Trends and the Role of Cation D Orbitals. *Appl. Phys. Lett.* **1998**, *72* (16), 2011–2013.

(68) Xue, D.-J.; Yang, B.; Yuan, Z.-K.; Wang, G.; Liu, X.; Zhou, Y.; Hu, L.; Pan, D.; Chen, S.; Tang, J. $CuSbSe_2$ as a Potential Photovoltaic Absorber Material: Studies from Theory to Experiment. *Adv. Energy Mater.* **2015**, *5* (23), 1501203.

(69) Zakutayev, A.; Caskey, C. M.; Fioretti, A. N.; Ginley, D. S.; Vidal, J.; Stevanovic, V.; Tea, E.; Lany, S. Defect Tolerant Semiconductors for Solar Energy Conversion. *J. Phys. Chem. Lett.* **2014**, *5* (7), 1117–1125.

TOC FIGURE